

## Analysis of effects of the state of charge on the formation and growth of the deposit layer on graphite electrode of pouch type lithium ion polymer batteries

Victor A. Agubra <sup>a,\*</sup>, Jeffrey W. Fergus <sup>a</sup>, Rujian Fu <sup>b</sup>, Song-Yul Choe <sup>b</sup>

<sup>a</sup> Materials Research and Education Center, Auburn University, 275 Wilmore Laboratories, Auburn, AL 36849, USA

<sup>b</sup> Department of Mechanical Engineering, Auburn University, 1418 Wiggins Hall, Auburn, AL 36849, USA



### HIGHLIGHTS

- Raising the battery state of charge increased the rate of side reaction.
- A significant amount of lithium was consumed in forming the deposit layer.
- Loss of carbon particles adhesion led to particles isolation in the electrochemical process.

### ARTICLE INFO

#### Article history:

Received 21 April 2014

Received in revised form

4 July 2014

Accepted 19 July 2014

Available online 24 July 2014

#### Keywords:

Lithium-ion cell

Graphite electrode

Electrolyte decomposition

Capacity fade

### ABSTRACT

The breakdown of the protective solid electrolyte interface (SEI) layer formed on lithium ion battery anodes can initiate further electrolyte decomposition and the formation of non-uniform and electronically insulating reaction products on the surface of the graphite particles. The results from this study indicate that raising both the lower and upper ends of the state of charge (SOC) increased the rate of the electrolyte decomposition side reaction to form a thick deposit surface film. This deposit layer contained lithium that can no longer participate in the reversible electrochemical reaction. In addition, the high cycling potential coupled with high charge rate created a large lithium concentration gradient that led to some particles detachment from the current collector and isolation in the electrochemical process.

© 2014 Elsevier B.V. All rights reserved.

## 1. Introduction

Cost effective implementation of lithium ion batteries requires long operational lifetimes, so various research groups have been exploring mechanisms that cause the lithium ion battery to lose its capacity [1–8]. Mechanisms such as loss of accessible lithium ions, degradation of electrodes, binder, corrosion of current collectors, and electrolyte decomposition to form an insoluble film between electrode and electrolyte interface have been reported as some of the main contributing factors to capacity fade [9–11].

A robust SEI layer prevents the occurrence of further electrolyte reduction on the carbon electrode, which is formed from the reduction of the electrolyte salt  $\text{LiPF}_6$  to produce a strong Lewis acid

$\text{PF}_5$  [12] that undergoes a ring-opening reaction with the solvent molecules in the presence of the  $\text{Li}^+$  to initiate its formation. This SEI layer is a  $\text{Li}^+$  conductor but an insulator to electron flow. However, at elevated temperature the metastable species  $\text{ROCO}_2\text{Li}$  within the SEI layer decomposes into more stable compounds  $-\text{Li}_2\text{CO}_3$  and  $\text{LiF}$ , which distort the SEI layer [13] and create a porous SEI structure that exposes the graphite surface to more electrolyte decomposition reaction [14]. The deposited layers lead to the loss/consumption of recyclable lithium ions at electrode/electrolyte interface and are one of the major causes of reversible capacity loss in the lithium ion battery.

In this article, a quantitative analysis of the effect of the state of charge (SOC) on the growth of the deposit layer on the anode electrode/electrolyte interface and a direct measurement of the loss of carbon particles resulting from diffusion induced stress during the intercalation/de-intercalation of lithium ion into the graphite structure are presented. The deposition due to solvent reduction

\* Corresponding author. Tel.: +1 3348443353; fax: +1 3348443400.

E-mail address: [vaa0002@auburn.edu](mailto:vaa0002@auburn.edu) (V.A. Agubra).

was observed only at the graphite electrode that on the cathode was considered negligible. Understanding the effects of the deposit layer on the lithium kinetics at the electrode/electrode interface and performance degradation is important.

## 2. Experimental

### 2.1. Battery chemistry

The batteries used in this study were the large format pouch type-lithium ion polymer batteries from battery manufacturer LGChem with a  $\text{Li}(\text{Mn},\text{Ni},\text{Co})\text{O}_2$  cathode and the anode material made of carbon with polyvinylidene fluoride (PVDF) as the binding material, with a composition of less than 3 wt% of the active material. The current collectors for anode and cathode electrode were copper and aluminum metals respectively. The batteries had a polymer electrolyte that consist of polyethylene oxide with lithium salt,  $\text{LiPF}_6$ , with co-solvents of ethylene carbonate (EC), and dimethyl carbonate (DMC). The nominal capacity of each battery is 15.7 Ah with an operating voltage level of 2.5–4.15 V. The complete battery were provided by the General Motors Company Ltd.

### 2.2. Cycling test

The charge/discharge cycles were performed using a in-house designed test station that comprised of a programmable charging system, a programmable electronic load system, a data acquisition system that are controlled by LabVIEW™ residing in a PC. The testing system allowed for the input of various charging conditions, such as C-rate, state of charge (SOC), and was located in an environmental chamber to allow for control of the external temperature. The batteries were charged by a constant current-constant voltage (CC–CV) charging protocol at room temperature. In each cycle, the cell was discharged with a constant current until the terminal voltage decreased to the voltage corresponding to the desired lower SOC and then charged with a constant current up to the voltage corresponding to the upper SOC followed by a constant voltage (CV) charge. A 4C charge and discharge current were used to accelerate the aging process. After every 20 cycles, a 1C discharge–resting–charge profile was applied to the cell to measure its capacity. The capacity ( $Q_{\max}$ ) was calculated by integrating the current when the cell was being discharged from 100% to 0% SOC using 1C current (15.7A) at room temperature. The  $Q_{\max}$  data for each battery were recorded every 20 cycles. The battery was rested for 10 min before and after the  $Q_{\max}$  measurement. The SOC levels; 5–70%, 15–80% and 25–90% were chosen to maintain a constant capacity of 65%. The pre-test terminal voltage for the desired SOC was determined by coulomb counting.

### 2.3. Electrochemical impedance spectroscopy (EIS)

A Gamry electrochemical impedance spectroscopy (EIS) framework in galvanostatic mode was used to apply different frequencies (1 mHz–1 kHz) of small AC excitation current (1 A) to battery and voltage responses were collected at 25 °C. The battery state of charge was maintained at 50% during the EIS test. A bipolar power supply was used to amplify the signal from EIS signal board. The measured impedances of the batteries were fit using the equivalent circuit model shown in Fig. 1 to find parameters such as the SEI film resistance, the Ohmic resistance, the charge transfer resistance, the double layer capacitance and Warburg impedance of the battery. In the model,  $R_0$  presents the Ohmic resistance caused by electrolyte, deposit layer, separator, current collector and electrode, which equals to the left intercept between impedance spectrum and the x-

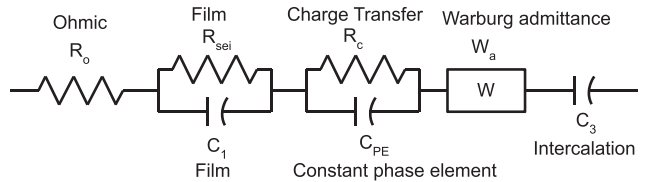


Fig. 1. Equivalent circuit model.

axis at high frequency ( $\approx 1$  kHz) [2].  $R_{sei}$  and  $C_1$  indicate SEI resistance and constant phase element (CPE) at anode [3], which dominate the shape of the first semi-circle in high frequency domain from 1 kHz to several Hz [4]. While  $R_c$  and  $C_2$  indicate charge transfer resistance and double layer capacitance, respectively. They affect the shape of the second semi-circle, which is less obvious in the lower frequency range (several Hz to several mHz) [3]. On the other hand,  $W_a$  is the Warburg admittance represents ion diffusion in the solid electrode and  $C_3$  is the intercalation capacitance that indicates the process of ion intercalation [3]. Both  $W_a$  and  $C_3$  dominate the impedance spectrum in the low frequency region (<several mHz). To extract these parameters, the EIS-ECM was fitted to the impedance spectrum measured by EIS using simplex algorithm.

### 2.4. Materials postmortem analysis

After cycling the batteries for 600 cycles and measurement of capacity and impedance, the battery was discharged to 0% SOC and dismantled in an argon atmosphere in glove box. The anode electrodes were harvested, cleaned in DMC and dried. A quantitative analysis of the thickness of the formed deposit layer was carried out by taking a cross sectional view (the samples were mounted on an epoxy and the edges polished) of the deposited surface layer and measuring its thickness using a scanning electron microscope (SEM) (Fig. 2). Four anode electrodes (out of a total 13 electrodes) from each condition were selected by visual examination to represent the range of the amount of deposit and area of carbon particles loss. Specifically, one electrode (out of 4) with heavy amounts of deposit/large area of carbon loss, one electrode (out of 3) with light amounts of deposit/small area carbon loss and two electrodes (out of 6) in-between these two extremes. Four samples were taken from each of the four selected electrodes, and for each sample, six different thicknesses of the deposited layer for each sample were measured. Therefore for each electrode, the thickness of the deposited layer was calculated by taken the mean value of the 24 measured thicknesses. Similarly, for the carbon particles loss area, the same numbers of electrodes and samples were used. The areas were measured by fitting the loss area with discrete circles or rectangles using annotate/measurement tool on the SEM. These areas were then calculated by averaging the areas of either the circles or the rectangles.

X-ray diffraction (XRD) spectra for the graphite anode electrode were obtained using a Bruker D8 to investigate the changes in the graphite crystal structure and the formation of any new phases. The composition of the deposit layer was also analyzed using Fourier transformed infra-red spectroscopy (FTIR) and X-ray photoelectron spectroscopy (XPS). For FTIR analysis, a Bruker optics equipped with single-reflection attenuated total reflection (ATR) accessory was used. The electrode samples were adjusted such that the beam was directly on the deposit layer area to ensure maximum absorbance. Each spectrum was recorded by accumulating 128 scans with a resolution of 4 cm. For XPS analysis, a VG ESCA scientific theta probe spectrometer was used.

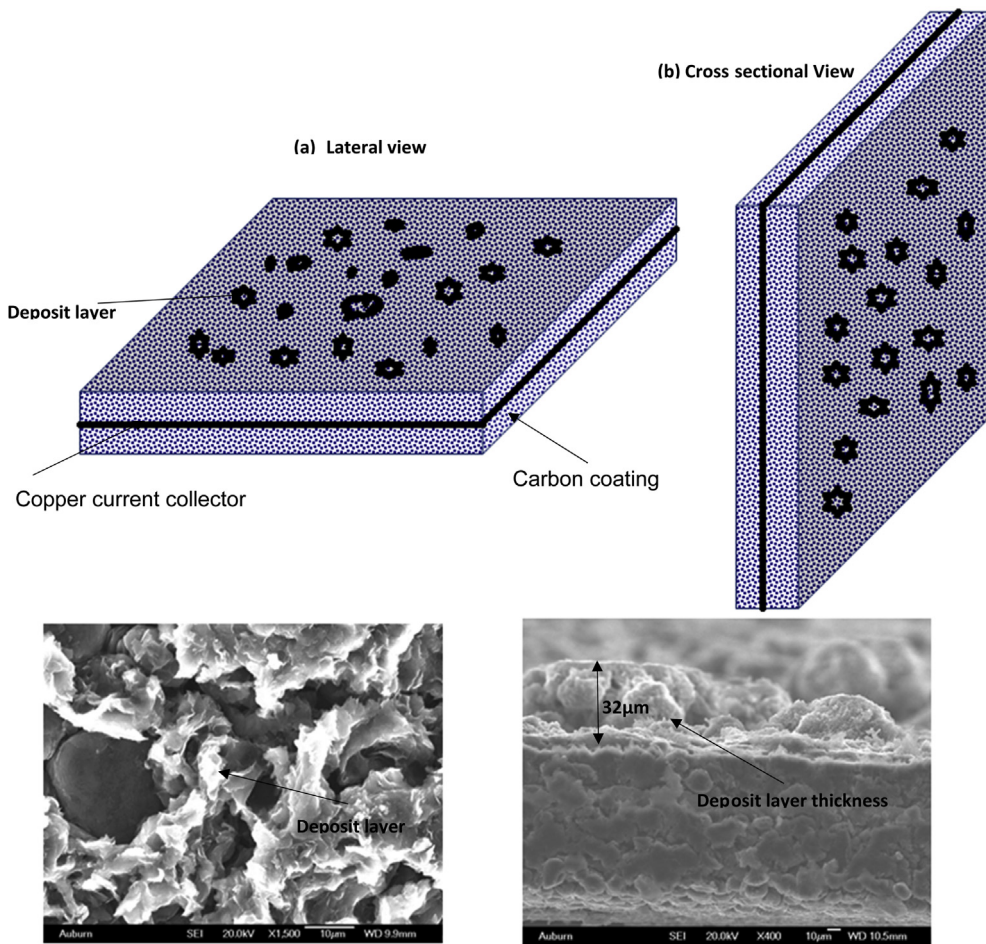


Fig. 2. Lateral and cross sectional view of the deposited surface layer.

Samples were prepared according to XPS sample standard (1 mm × 1 mm) and transferred to the XPS spectrometer inside an argon-filled sample box. The carbon 1s peak at 285 eV was used as the binding energy scale reference, and the Ag 3d5/2 line at 368 eV with full width at half maximum (FWHM) of 0.66 eV was used to calibrate the spectrometer. To achieve high-resolution spectra, a constant pass energy of 50 eV was used and the pressure in the analysis chamber was maintained at  $6 \times 10^9$  mbar. Data analyses were performed using Gaussiane Lorentzian curve fitting with Shirley background subtraction.

### 3. Results and discussion

#### 3.1. Electrochemical

The measured  $Q_{\max}$  values of the batteries for up to 600 cycles are plotted in Fig. 3. The  $Q_{\max}$  values for both 25%–90% and 15%–80% SOC levels were similar and loss of the capacity was 17% after 600 cycles, while the capacity fade for 5%–70% was only 7.8%. The high irreversible capacity loss at high battery cycling potential is consistent with the findings of Jiang et al. [15]. However, the capacity loss in their study was attributed to structural changes in both electrodes and large entropy change. To elucidate the causes of these irreversible capacity losses in this study, materials analysis of the harvested anode electrode were carried out.

#### 3.2. Anode electrode materials characterization

##### 3.2.1. Deposit layer formation

SEM micrographs of the surface morphology of anode electrodes before and after aging are shown in Fig. 4a. On the surface of the aged anode electrodes are the decomposition reaction products

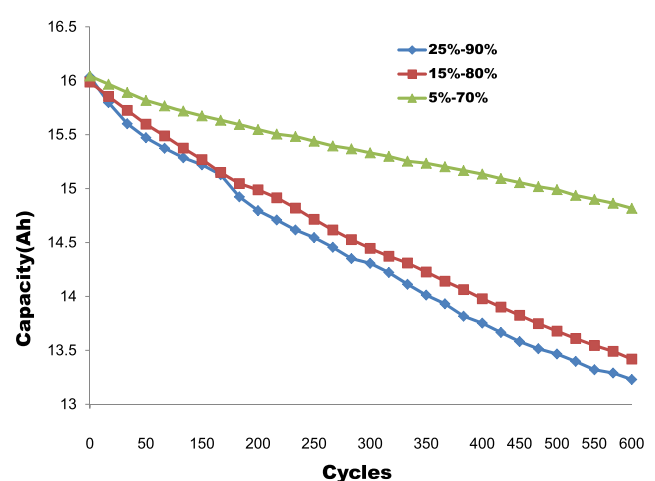
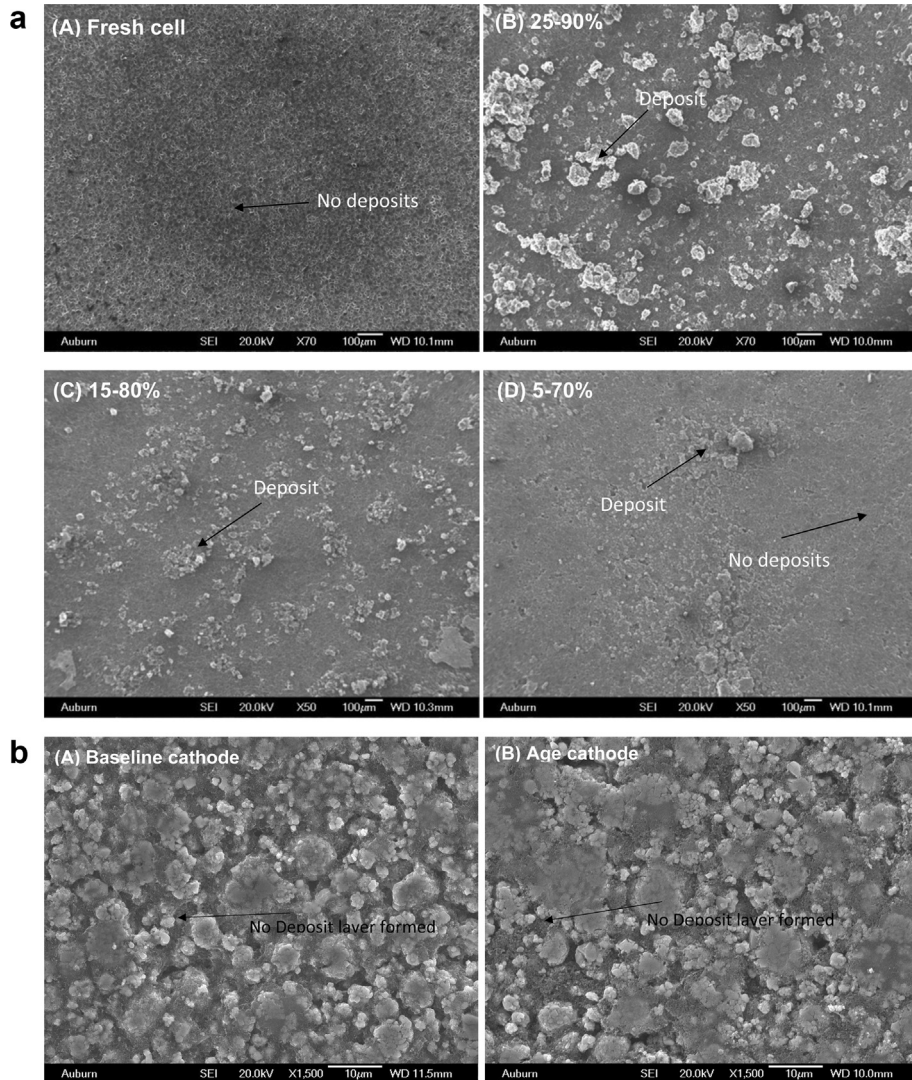
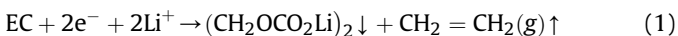


Fig. 3. Capacity fade of batteries cycled at over different states of charge.

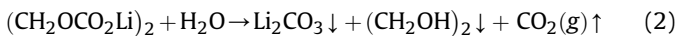


**Fig. 4.** a: Morphology of deposit surface film layer on the anode electrode for cells cycled at 600 cycles over different SOC ranges. b: Morphology of the baseline and aged cathode electrode after 600 cycles.

deposited on the surface of the graphite particles. The morphology of the aged cathode (Fig. 4b) did not differ from the baseline (fresh cell), therefore the deposition due to solvent reduction reaction on the cathode/electrode interface was considered negligible. Various studies [16,17] indicate that the highly reactive electrolyte solvent, ethylene carbonate (EC), undergoes a two electron reduction. In a mixture with other carbonate solvents, the ethylene carbonate (EC) is preferably reduced due to its high polarity and dielectric constant [18]. The reduction of EC thus involves a two-electron transfer to one mole EC molecules and reaction with  $\text{Li}^+$  to produce  $\text{Li}_2\text{CO}_3$  and  $\text{C}_2\text{H}_4$  gas (Eq. (1))



The species  $(\text{CH}_2\text{OCO}_2\text{Li})_2$  on the graphite particles surface, can readily react with traces of  $\text{H}_2\text{O}$  in the solution to produce  $\text{Li}_2\text{CO}_3$ ,  $(\text{CH}_2\text{OH})_2$  and  $\text{CO}_2$  gas (Eq. (2)) [19,20].



These species form the solid electrolyte interface (SEI) on the anode electrode. However, the distortion of the SEI layer structure

due prolong cycling exposes the graphite surface to more electrolyte decomposition reaction [8,9]. In particular, the decomposition species of  $\text{POF}_3$  and  $\text{PF}_6^-$  from the unstable salt  $\text{LiPF}_6$  reduction react with EC to produce various species on the anode electrode (Eq. (3)) [21].



The EC reduction process continue to produce a Lewis acid or salt anion (Eq. (4)) at each subsequent reduction step that perpetuate the electrolyte reduction process.



Therefore at high SOC, these electrolyte decomposition reactions resulted in the formation and growth of the deposit layer on the surface of the graphite electrode (Fig. 5) to form a non-uniform agglomerates. The presence of these reaction products on the surface could block the pores of the anode electrode and impact negatively on the intercalation kinetics at the electrode/electrolyte interface. Fig. 4a shows that the sizes and amounts of these agglomerates were dependent upon SOC and higher for the higher SOC levels, which could be due to the increased electrolyte decomposition at the

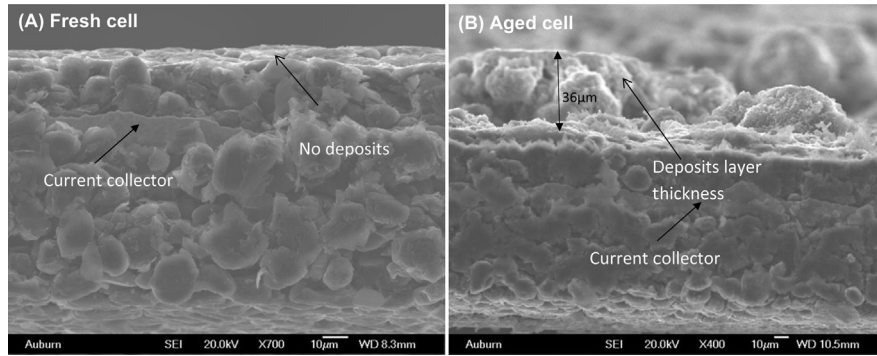


Fig. 5. Thickness of deposit layer as observed from an aged anode electrode at 600 cycles.

higher potential during charging. At the low SOC level 5%–70%, the deposit layers were isolated. A physical examination of the electrolyte between the separator/electrolyte interfaces showed a drier separator for the cells tested at 25%–90% SOC compared to those tested at 5%–70% SOC, which was also an indication of the depletion of electrolyte used in the decomposition reaction. The surface analysis of the deposit layer from the XPS analysis showed that the deposit layer contained lithium that was not available for further electrochemical reaction. Therefore a continuous electrolyte decomposition will result in the depletion of recyclable lithium.

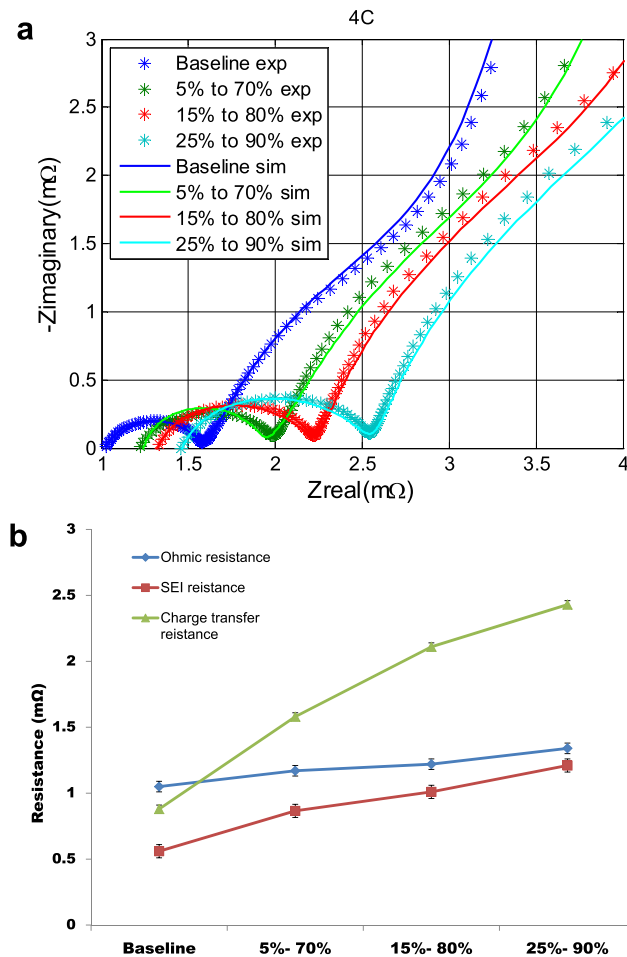


Fig. 6. a: Experimental and simulated Impedance plots of aged batteries for the different state of charge range for batteries cycled at 600 cycle. b: Resistance of the LiB for different SOC extracted from the equivalent circuit model.

### 3.2.2. Effects of deposited surface layer

Lithium ion batteries employ particles with pores to increase the active area between the electrolyte and the electrode to facilitate the electrochemical reaction process. A deposit layer on the surface of the active carbon materials will block the electrode pores and also decrease the active surface area of the electrode. This inadvertently the lithium kinetics at the electrode/electrolyte interface, which increased the overall battery impedance. The Nyquist plots

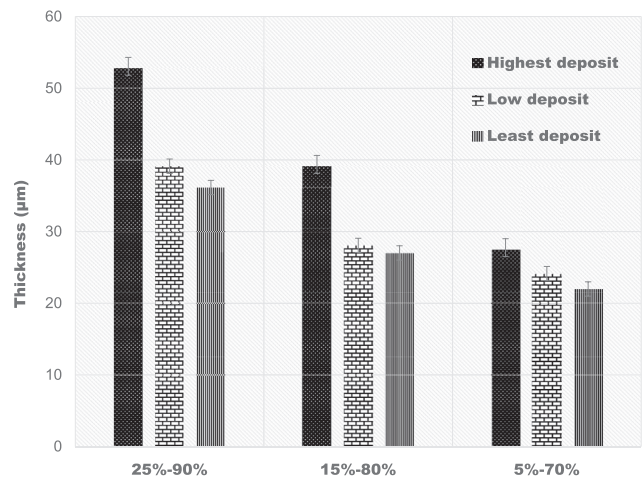


Fig. 7. Thickness of the deposit layer measured from SEM micrographs of aged anode electrode after 600 cycles.

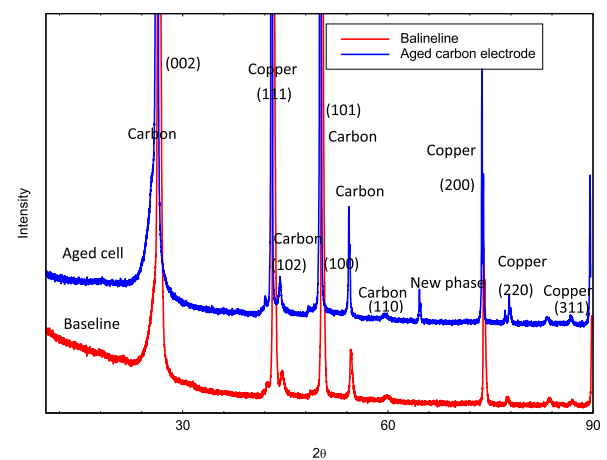
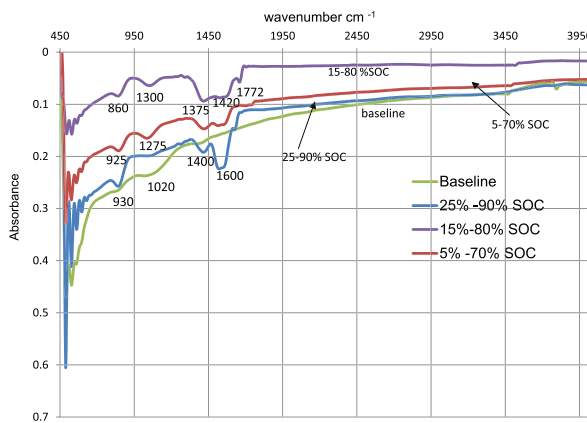


Fig. 8. X-rays diffraction spectra for aged and baseline for the anode electrode.



**Fig. 9.** FTIR of surface compounds of the deposit surface layer for aged anode electrode after 600 cycles.

of the experimental impedance spectroscopy along the equivalent model fits results for the different SOC levels are shown in Fig. 6a.

The plots consist of two parts, a semicircle and a linearly increasing slope. The radius of the semicircle presents the SEI resistance, while the slope is mostly determined by diffusion effects of ions in solid. The increase in radius of the semicircles with cycling implies a growth of SEI layer and the amount of this growth is larger as the SOC level increases. At the same time, the high frequency intercept, which corresponds to the Ohmic resistance, increases with cycling due to the decrease of ion conductivity of the electrolytes. The overall battery impedance is comprised of many specific battery component/interface resistances; the  $\text{Li}^+$  charge transfer resistance between graphite/electrolyte interface ( $R_c$ ), the Ohmic resistance ( $R_o$ ) and the SEI layer resistance ( $R_{\text{sei}}$ ). To extract

these resistances, an equivalent circuit model (Fig. 1) based on the impedance characteristics was used to extract these parameters that represented different electrochemical properties of the battery. The extracted parameters of resistances are plotted in Fig. 6b. The resistances tend to increase as the lower and upper end of the SOC were raised. Particularly, the increase in the charge transfer resistance was the largest. The increases with increasing SOC level could be due to the formation of the deposited surface layer on the graphite particles, which formed greater amounts for the higher SOC level.

### 3.2.3. Growth of the deposited surface layer

The thicknesses of the deposited surface film layer observed among the different SOC levels were measured from cross sectional views of the anode electrode as shown in Fig. 5 and are plotted in Fig. 7 for the various SOC levels. The measured deposit layer thickness showed an average thickness of 53  $\mu\text{m}$  for the most affected deposit electrode for the high SOC range (25–90%) compared to 39  $\mu\text{m}$  for the 15–80% SOC range, and 27  $\mu\text{m}$  for the low SOC range (5–70%). For the least deposit affected electrodes, the 25–90% SOC range recorded an average of deposit thickness of 36  $\mu\text{m}$ , 27  $\mu\text{m}$  for the 15–80% SOC, and 21  $\mu\text{m}$  for the low SOC range (5–70%). The growing deposit layer created a barrier for charge transfer at the graphite/electrolyte interface [22] and cause the observed increase in charge transfer resistance.

### 3.2.4. Composition of the deposited layer

X-ray diffraction for the aged anode indicated a new phase with a peak at  $2\theta = 64^\circ$  (Fig. 8) in addition to those peaks patterns for the carbon and the copper current collector, which was attributed to the presence LiF species from the analysis of JCPDS card from Ref. [23]. The deposited surface film was analyzed further with FTIR to identify the surface compounds constituting the deposited surface

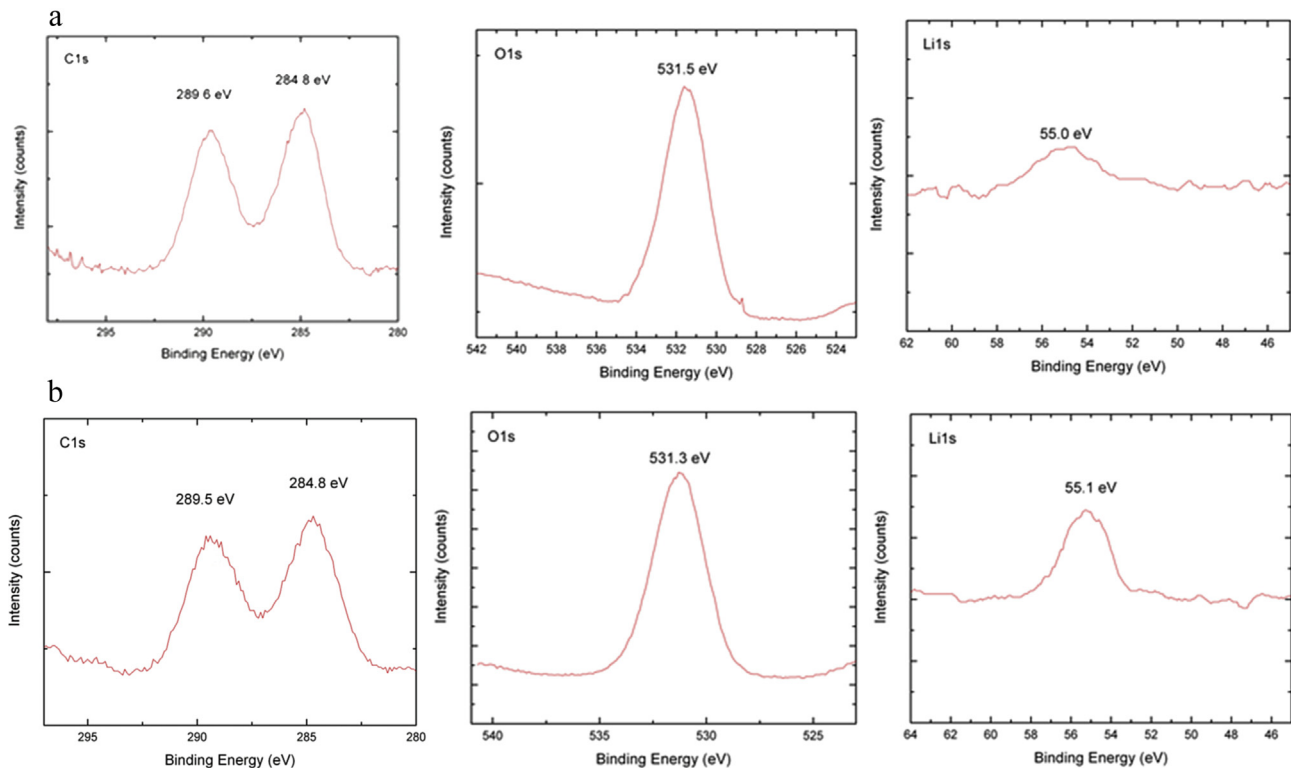


**Fig. 10.** a: High resolution XPS spectra over the C1s, O1s, and Li1s portions regions from the baseline cell. b: High resolution XPS spectra over the C1s, O1s, and Li1s portions regions from aged 25–90% SOC at 4C cell.

**Table 1**

XPS elemental surface layer composition for the baseline/aged battery (At %).

Condition	Li	C	O	F
Baseline cell	40	26	33	1
Aged cell	44	26	28	2

film layer. As shown in **Fig. 9**, the absorption bands at  $1750\text{ cm}^{-1}$  represent the stretching vibration of  $\text{C}=\text{O}$  in EC, while those at  $1300\text{ cm}^{-1}$  and  $1450\text{ cm}^{-1}$  are the asymmetric stretching vibration of the  $\text{C}-\text{O}-\text{C}$  and  $\text{CH}_2$  bending vibration of decomposition products of the electrolyte solution, respectively [24]. The main chemical constituents of the SEI layer in the  $\text{LiPF}_6$ –EC/DMC solution are  $\text{ROCO}_2\text{Li}$  and  $\text{Li}_2\text{CO}_3$  [25], which generally have spectra at  $1600\text{ cm}^{-1}$  and  $1300\text{ cm}^{-1}$  for  $\text{ROCO}_2\text{Li}$  and  $860\text{ cm}^{-1}$  and  $1375\text{ cm}^{-1}$  for  $\text{Li}_2\text{CO}_3$ . The FTIR analysis indicates that the chemical constituents of the deposited surface film layer are the same as those in the SEI layer from the electrolyte decomposition reaction lithium on the surface of the anode electrode.

From the XPS analysis, the baseline spectrum for the carbon anode clearly shows a graphite peak at  $284.5\text{ eV}$  (**Fig. 10a**). A small peak in the  $290$ – $291\text{ eV}$  range corresponds to the  $\text{C}-\text{F}$  bond in the PVDF binder materials. The peak at  $533\text{ eV}$  was the most prominent peak in the  $\text{O}1\text{s}$  spectra for the aged anode electrode (**Fig. 10b**). Furthermore,  $\text{Li}_2\text{CO}_3$  (expected at  $531.5\text{ eV}$ ), and species like  $\text{Li}_2\text{O}$  and  $\text{LiOH}$  (expected  $<530\text{ eV}$ ) were detected in the  $\text{O}1\text{s}$  spectra. An increase in the peak of the  $\text{Li}1\text{s}$  at  $55.1\text{ eV}$  for the aged electrode

was consistent with the existence of  $\text{LiF}$  species on the deposit layer. The electrolyte contains impurities such as  $\text{H}_2\text{O}$  and oxygen, which can lead to the formation of  $\text{LiOH}$  and  $\text{Li}_2\text{O}$ . The lithium amount in the baseline and the aged battery were similar as shown in **Table 1**. The XPS signal is limited to  $1$ – $2\text{ nm}$ , so this composition represented the outer surface of the deposit layer.

### 3.2.5. Loss of carbon particles

**Fig. 11a** shows that the carbon particles were detached from the carbon electrode indicating that there was a loss of adhesion between carbon particles and between carbon particles and the current copper collector on the anode electrode. The volume changes associated with lithium intercalation/de-intercalation into the graphite structure results in particle expansion/contraction [26] which could generate diffusion induced stresses and cause loss of adhesion of the binding material between the particles and particle and the current collector. As a result, some of the active carbon particles could be isolated from the electron-conducting matrix of the electrode and thus became inactive in the electrochemical process. The loss area of these isolated carbon particles were measured and plotted for the different SOC levels for the largest loss electrode in **Fig. 11b**. The higher SOC range (25–90%), in particular had the largest amount of carbon particles loss, and this loss decrease progressively as the SOC range was reduced. However, this loss in carbon particles area as a percentage of the total surface area of the anode electrode, amounted to about 1% at 25%–90% SOC level, and an even smaller area loss for the lower SOC level.

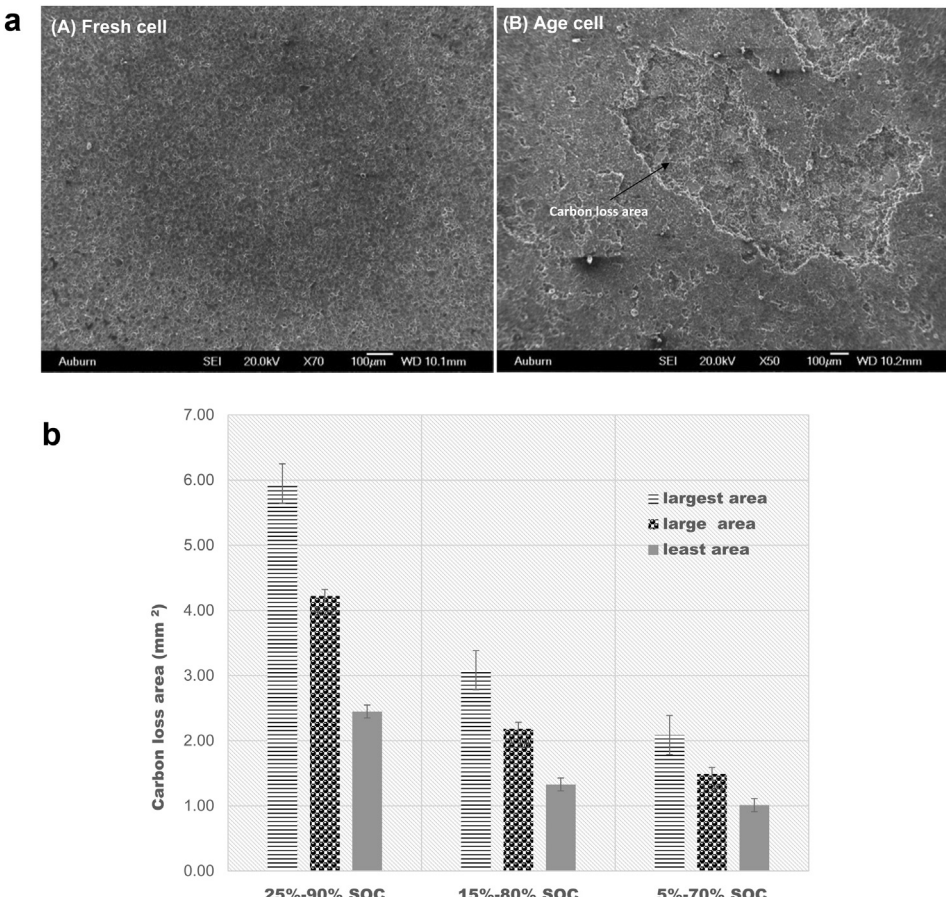


**Fig. 11.** a: Loss of carbon particles adhesion on the surface of the graphite anode after 600 cycles. b: Loss area measurement of carbon particles for cells cycled at 600 cycles for the different SOC.

However, this particle loss could significantly increase for prolonged higher cycle numbers.

#### 4. Conclusions

Increasing the SOC level (both the lower and upper end of the SOC level) resulted in formation of thick deposit layer from side reaction. This deposit layer contained lithium that was not available for further electrochemical reaction. The layer at the electrode/electrolyte interface contributed to the increase charge transfer resistance. The high SOC level coupled with a high charge rate led to loss and isolation of carbon particles. The loss of carbon particles adhesion was attributed to cycling the batteries at high charge rate that caused a large lithium concentration gradient that leading to some particles isolation in the electrochemical process. These factors contributed to the loss of reversible battery capacity.

#### Acknowledgment

This project is funded by General Motors Corporation, USA. The authors do appreciate the financial support and technical discussions.

#### References

- [1] S. Kong, B. Kim, W. Yoon, *J. Electrochem. Soc.* 159 (2012) A1551–A1553.
- [2] R. Bhattacharyya, B. Key, H. Chen, A.S. Best, A.F. Hollenkamp, C.P. Grey, *Nat. Mater.* 9 (2010) 504–510.
- [3] J. Zheng, X. Wu, Y. Yang, *Electrochim. Acta* 105 (2013) 200–208.
- [4] W. Lu, M. Carmen, N. Liu, T.J. Vaughn, A. Jansen, D.W. Dees, *J. Electrochem. Soc.* 159 (2012) A566–A570.
- [5] J. Fan, S. Tan, *J. Electrochem. Soc.* 153 (2006) A1081–A1092.
- [6] F. Joho, B. Rykart, R. Imhof, P. Novak, M.E. Spahr, A. Monnier, *J. Power Sources* 81 (1999) 243–247.
- [7] C. Natarajan, H. Fujimoto, K. Tokumitsu, A. Mabuchi, T. Kasuh, *Carbon* 39 (2001) 1409–1413.
- [8] S.S. Choi, H.S. Lim, *J. Power Sources* 111 (2002) 130–136.
- [9] G. Ning, B. Haran, B.N. Popov, *J. Power Sources* 117 (2003) 160–169.
- [10] M. Dolle, L. Sannier, B. Beaudion, M. Trentin, *J. Electrochem. Soc.* 5 (2002) A286–A289.
- [11] M. Wolfgang, C. Lu, P. Novak, *J. Electrochem. Soc.* 158 (2011) A1478–A1482.
- [12] N.N. Sinha, T.H. Marks, H.M. Dahn, A.J. Smith, J.C. Burn, D.J. Coyle, J.J. Dahn, J.R. Dahn, *J. Electrochem. Soc.* 159 (2012) A1672–A1681.
- [13] W. Li, C. Campion, L.B. Lucht, B. Ravdel, J. Dicarlo, K.M. Abraham, *J. Electrochem. Soc.* 152 (2005) A1361–A1365.
- [14] S.B. Lee, S. Pyun, *Carbon* 40 (2002) 2333–2339.
- [15] J. Jiang, W. Shi, J. Zheng, P. Zuo, J. Xiao, X. Chen, W. Xu, J.G. Zhang, *J. Electrochem. Soc.* 161 (2014) A336–A341.
- [16] M.D. Levi, C. Wang, J.S. Gnanara, D. Aurbach, *J. Power Sources* 119 (2003) 538–542.
- [17] P. Moss, G. Au, E. Plichta, J. Zheng, *J. Electrochem. Soc.* 157 (2010) A1–A7.
- [18] Y. Okamoto, *J. Electrochem. Soc.* 160 (2) (2013) A404.
- [19] R. Dedryvère, H. Martinez, S. Leroy, D. Lemordant, F. Bonhomme, P. Biensan, D. Gonbeau, *J. Power Sources* 174 (2007) 462–468.
- [20] D. Aurbach, M. Mashkovich, *J. Electrochem. Soc.* 145 (8) (1998) A2629.
- [21] F. Joho, P. Novák, *Electrochim. Acta* 45 (2000) 3589–3599.
- [22] G. Ning, B. Haran, B. Popov, *J. Power Sources* 117 (2003) 160–169.
- [23] Swanson, Tatge, Natl. Bur. Stand US Cir. 539 (1) (1953) 61.
- [24] C. Huang, S. Zhuang, F. Tu, *J. Electrochem. Soc.* 160 (2013) A376–382.
- [25] S.I. Pyun, Y.G. Ryu, *J. Electroanal. Chem.* 455 (1998) 11–17.
- [26] R. Bouchet, S. Lascaud, M. Rosso, *J. Electrochem. Soc.* 150 (2003) A1385–A1389.